Configuration-sensitive transport at the domain walls of a magnetic topological insulator

Yan-Feng Zhou, Zhe Hou, and Qing-Feng Sun

Phys. Rev. B **98**, 165433 — Published 23 October 2018

DOI: 10.1103/PhysRevB.98.165433

Configuration-sensitive transport on domain walls of a magnetic topological insulator

Yan-Feng Zhou[1,2], Zhe Hou[1,2], and Qing-Feng Sun[1,2,3*]
[1] *International Center for Quantum Materials, School of Physics, Peking University, Beijing 100871, China*
[2] *Collaborative Innovation Center of Quantum Matter, Beijing 100871, China and*
[3] *CAS Center for Excellence in Topological Quantum Computation, University of Chinese Academy of Sciences, Beijing 100190, China*
(Dated: October 4, 2018)

We study the transport on the domain wall (DW) in a magnetic topological insulator. The low-energy behaviors of the magnetic topological insulator are dominated by the chiral edge states (CESs). Here, we find that the spectrum and transport of the CESs at the DW are strongly dependent on the DW configuration. For a Bloch wall, two co-propagating CESs at the DW are doubly degenerate and the incoming electron is totally reflected. However, for a Néel wall, the two CESs are split and the transmission is determined by the interference between the CESs. Moreover, the effective Hamiltonian for the CESs indicates that the component of magnetization perpendicular to the wall leads to the distinct transport behaviors. These findings may pave a way to realize the low-power-dissipation spintronics devices based on magnetic DWs.

I. INTRODUCTION

The discovery of topological insulator (TI) has attracted intensive interest in searching for topologically non-trivial states of condensed matter and subsequently, triggered a series of occurrences of novel physical effects[1,2]. The quantum anomalous Hall effect (QAHE), i.e., quantum Hall effect without the external magnetic field, can be achieved in magnetic TIs by introducing ferromagnetism in TIs.[3,4] The magnetic TI has an insulating bulk classified by a Chern number $\mathcal{C}$ and $\mathcal{C}$ conducting chiral edge states (CESs) through bulk-boundary correspondence. In recent, QAHE has been experimentally realized in Cr-doped[5–9] and V-doped[10] $(\mathrm{Bi,Sb})_2\mathrm{Te}_3$ magnetic TI thin films, and the Hall resistance shows a quantized value $\pm h/e^2$ implying that the Chern number of the magnetic TIs $\mathcal{C}=\pm1$ which can be controlled by the magnetization direction[11].

The boundary between magnetic TI domains of opposite magnetization with $\mathcal{C}=\pm1$ forms a magnetic domain wall (DW) as shown in Fig.1(a). The total magnetic energy of the magnetic materials consist of the exchange interaction, magnetic anisotropy and the dipolar interaction. A continuous change of the magnetization leading to the DWs is inherent to magnetic materials to minimize the total magnetic energy rather than a sharp change. Both the optimized configuration and thickness of the DW are determined by a balance between competing energy contributions[12,13]. Two energetically favorable configurations are Bloch wall and Néel wall, and the transition between the two configurations can be controlled by Dzyaloshinskii-Moriya interaction[14–17]. Moreover, due to the different chirality of CESs across the DW, two co-propagating CESs are expected to reside on the DW. Very recently, the DWs of magnetic TI have been realized in Cr-doped $(\mathrm{Bi,Sb})_2\mathrm{Te}_3$ by the tip of a magnetic force microscope[18] and by spatially modulating the external magnetic field using Meissner repulsion from a bulk superconductor[19], and the chiral transport of CESs has been observed in these experiments. Owing to the robustness of the CESs against backscattering, the DWs of magnetic TIs have potential applications in low-power-consumption spintronic devices, such as the nonvolatile racetrack memory[20].

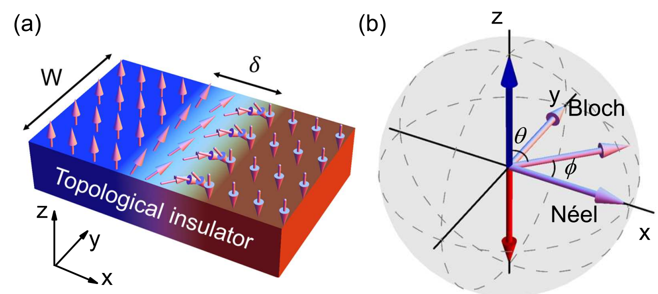

FIG. 1. (a) Schematic diagram of a magnetic DW between two magnetic TI domains. Here the magnetic DW is in the y direction at $x=0$. The magnetization vector $\mathbf{M}(x)$ is homogeneous away from the DW and it points to $+z$ $(-z)$ direction for $x \ll 0$ $(x \gg 0)$. The direction of $\mathbf{M}(x)$ rotates continuously from $+z$ to $-z$ direction inside the DW. (b) The sphere of possible $\mathbf{M}$ with the magnetization configurations corresponding to the different rotation modes defined by the azimuthal angle ϕ. Here $\phi=0$ and $\pi/2$ corresponds to Néel wall and Bloch wall, respectively.

In this paper, we study the transport of a two-terminal device containing a DW of thickness δ and width W in a magnetic TI [see Fig.1(a)]. In the low energy case, the transport behaviors of the magnetic TI are dominated by CESs at the device edges as well as at the DW. We calculate the band structures of magnetic TIs with both a Bloch wall and a Néel wall. For a Bloch wall, two co-propagating linear CESs at the DW are doubly degenerate, while for a Néel wall a split is present. As a result, the transport property is strongly dependent on the DW configuration. In the Bloch wall case, the incoming electron with zero energy is totally reflected regardless of the system parameters. However, in the Néel case, the device functions as a chirality-based Mach-Zehnder interferometry, so that the transmission coefficient oscillates between zero and unity with changes in system parameters. Moreover, we find that the electrical transport of the CESs is robust against the disorders for both Néel and Bloch walls. By constructing the scattering matrix of the device from the effective Hamiltonian, these transport behaviors can be well understood.

The rest of the paper is organized as follows. After this introductory section, Sec. II provides the model describing the configuration of magnetic DWs and the Hamiltonian determining the properties of the considered system. Then, we calculate the band structure of CESs residing at the DW of a magnetic TI in Sec. III A and derive one-dimensional effective Hamiltonian of the CESs in Sec. III B for both Néel and Bloch walls from the Hamiltonian given in Sec. II. In Sec. IV, the transport properties of the magnetic TI via the CESs are studied numerically by nonequilibrium Green's function method and can be understand by the scattering matrix constructed from the one-dimensional effective Hamiltonian. Sec. V concludes this paper. Some auxiliary materials are relegated to Appendix.

II. MODEL AND HAMILTONIAN

As shown in Fig.1(a), two magnetic TI domains with upward (blue region) and downward (red region) magnetization are separated by a DW. The magnetization vectors are homogeneous away from the DW and change continuously from $+z$ direction to $-z$ direction inside the DW. The configuration of the DW can be described by magnetization vector $\mathbf{M}(x) = (M_x, M_y, M_z) = M(\sin\theta\cos\phi, \sin\theta\sin\phi, \cos\theta)$, with a constant magnitude M originated from magnetic doping.[18] The azimuthal angle θ is a function of x with $\cos\theta(x) = -\tanh\frac{x}{\delta}$ and the azimuthal angle ϕ defines the type of the magnetic DW. From the sphere of possible magnetization vectors, the azimuthal angle of magnetic vectors is $\phi = 0$ in Néel wall and $\phi = \pi/2$ in Bloch wall respectively [see Fig.1(b)].

The low-energy states of magnetic TI can be described by the Hamiltonian[4,21,28] $H = \sum_{\boldsymbol{k}} \Psi_{\boldsymbol{k}}^\dagger H(\boldsymbol{k}) \Psi_{\boldsymbol{k}}$ with

$$H(\boldsymbol{k}) = \nu_F k_y \sigma_x \tau_z - \nu_F k_x \sigma_y \tau_z + m(\boldsymbol{k})\tau_x + \boldsymbol{M}\cdot\boldsymbol{\sigma}, \quad (1)$$

where the momentum $\boldsymbol{k} = (k_x, k_y)$ and $\Psi_{\boldsymbol{k}} = [\psi_{t\uparrow}, \psi_{t\downarrow}, \psi_{b\uparrow}, \psi_{b\downarrow}]^T$ being a four-component electron operator, where t and b label electrons from the top and bottom layers, and $\uparrow$ and $\downarrow$ denote electrons with spin up and down, respectively. $\sigma_{x,y,z}$ and $\tau_{x,y,z}$ are Pauli matrices for spin and layer. $m(\boldsymbol{k}) = m_0 - m_1(k_x^2 + k_y^2)$ describes the coupling between the top and bottom layers. As $M > m_0$, the magnetic TIs with Chern number $\mathcal{C} = \pm 1$ are realized in the domains with homogeneous upward and downward magnetization. For the numerical calculation, we discretize the Hamiltonian in Eq.(1) into

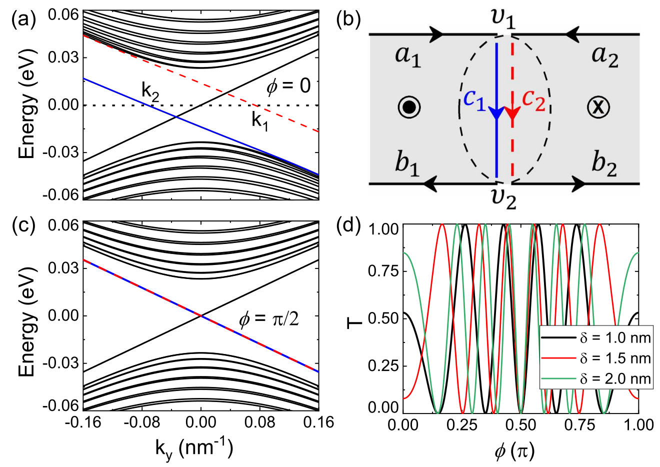

FIG. 2. (a) and (c) The band structures of an infinite slab of magnetic TI extending along the y direction with a Néel wall ($\phi = 0$) in (a) and Bloch wall ($\phi = \pi/2$) in (c). The width of the slab is 180.6 nm and the thickness of the DW is 1 nm. The blue solid and red dashed lines represent the chiral modes on the DW. (b) Schematic depicting the transport process based on the chiral modes. (d) The zero-energy transmission coefficient T of the device in Fig.1(a) versus ϕ for several DW thicknesses δ with the widths $W = 90$ nm.

a lattice version[23–26],

$$H = \sum_{\mathbf{i}} [\Psi_{\mathbf{i}}^\dagger T_0 \Psi_{\mathbf{i}} + (\Psi_{\mathbf{i}}^\dagger T_x \Psi_{\mathbf{i}+\delta\mathbf{x}} + \Psi_{\mathbf{i}}^\dagger T_y \Psi_{\mathbf{i}+\delta\mathbf{y}} + \text{H.c.})], \quad (2)$$

with $T_0 = (m_0 - 4\frac{m_1}{a^2})\tau_x + \boldsymbol{M}\cdot\boldsymbol{\sigma}$, $T_x = \frac{m_1}{a^2}\tau_x + \frac{i\nu_F}{2a}\sigma_y\tau_z$ and $T_y = \frac{m_1}{a^2}\tau_x - \frac{i\nu_F}{2a}\sigma_x\tau_z$ with a lattice constant $a = 0.6$ nm. Here $\Psi_{\mathbf{i}} = [c_{\mathbf{i}t\uparrow}, c_{\mathbf{i}t\downarrow}, c_{\mathbf{i}b\uparrow}, c_{\mathbf{i}b\downarrow}]^T$ is a four-component electron operator on site $\mathbf{i}$. $\delta\mathbf{x}$ ($\delta\mathbf{y}$) is the unit vector along x (y) direction. In the calculation, we set the Fermi velocity $\nu_F = 0.222$ eVnm, $m_0 = 0.026$ eV, $m_1 = 0.137$ eVnm^2, and $M = 0.048$ eV.[22]

III. CHIRAL EDGE STATES ON THE MAGNETIC DW

A. Numerical calculation of band structure

First, we study the spectrum of the CESs in an infinite slab of magnetic TI containing a DW [see Fig.1(a)] which extends along the y direction and has a finite width in x direction. In the calculation, the band structure is calculated numerically from the Hamiltonian in Eq. (2) and the open boundary condition is used along the x direction. As the slab is invariant by translating along the y axis, the momentum k_y is a good quantum number. Figures 2(a) and 2(c) show the band structures of the slab with a Néel wall ($\phi = 0$) and a Bloch wall ($\phi = \pi/2$), respectively. Inside the bulk gap, there are four linear chiral modes with two co-propagating modes along the

DW (blue solid and red dashed lines) and two degenerate modes along the slab edges propagating in opposite directions (black solid lines). The presence of two chiral modes residing on the DW arises from the change in Chern number from +1 to -1 across the DW. For Bloch wall, the co-propagating modes on the DW are degenerate, while for Néel wall, the chiral modes are split with energy dispersions $E \propto -k_y \pm \Delta k/2$. As the DW is located inside the slab, it has no effects on the chiral modes on the edges as shown in Fig.2(a) and (c).

B. One-dimensional effective Hamiltonian for the CESs

To make the split clear, let us construct the one-dimensional effective Hamiltonian for the co-propagating chiral modes on the DW. By a unitary transformation

$$U = \frac{1}{\sqrt{2}} \begin{pmatrix} 1 & 0 & 1 & 0 \\ 0 & 1 & 0 & -1 \\ 0 & 1 & 0 & 1 \\ 1 & 0 & -1 & 0 \end{pmatrix}, \tag{3}$$

the Hamiltonian (1) becomes

$$H'(k) = \begin{pmatrix} H_+ & M_\parallel \\ M_\parallel^\dagger & H_- \end{pmatrix}, \tag{4}$$

with

$$H_\pm = \nu_F k_y \tilde{\sigma}_x \mp \nu_F k_x \tilde{\sigma}_y + (m(k) \pm M_z)\tilde{\sigma}_z, \tag{5}$$

in terms of new bases $(\psi_{+\uparrow}, \psi_{-\downarrow}, \psi_{+\downarrow}, \psi_{-\uparrow})^T$ with $\psi_{\pm\uparrow} = (\psi_{t\uparrow} \pm \psi_{b\uparrow})/\sqrt{2}$ and $\psi_{\pm\downarrow} = (\psi_{t\downarrow} \pm \psi_{b\downarrow})/\sqrt{2}$, and $M_\parallel = M_x - iM_y\sigma_z$. $\tilde{\sigma}_{x,y,z}$ are Pauli matrices. Inside the DW with magnetization vector $\mathbf{M}(x) = M(\mathrm{sech}\frac{x}{\delta}\cos\phi, \mathrm{sech}\frac{x}{\delta}\sin\phi, -\tanh\frac{x}{\delta})$, both H_+ and H_- are nontrivial due to the sign change of M_z across the DW, so that there exist two chiral states[27,28]. As $H_\pm$ are coupled by element $M_\parallel$ in Eq.(4), to find the solutions of chiral states, we replace $k_x \to -i\partial_x$ and decompose the Hamiltonian as $H' = H_0 + \Delta H$, in which H_0 contains the decoupled $H_\pm$ and ΔH consists of the element $M_\parallel$. We solve H_0 first and treat ΔH as a perturbation[29,30].

First, we solve the eigenequation $H_+\zeta_+(x) = E\zeta_+(x)$ for $k_y = 0$ and $E = 0$. It can be checked that $H_+(k_y = 0)$ and $\tilde{\sigma}_x$ satisfy the anticommutation relation $\{H_+(k_y = 0), \tilde{\sigma}_x\} = 0$. Thus, the zero-energy eigenstate is the simultaneous eigenstate of H_+ and $\tilde{\sigma}_x$. Consider the ansatz $\zeta_+(x) = \eta_+^s(x)\chi_x^s$, where $\tilde{\sigma}_x\chi_x^s = s\chi_x^s$, $s = \pm 1$, and $\chi_x^s = (1, s)^T$ up to a normalized constant, we have

$$(s\nu_F\partial_x + m_0 + m_1\partial_x^2 + M_z)\eta_+^s(x) = 0. \tag{6}$$

With a substitution $u = (1 + e^{2x/\delta})^{-1}$,[31] we arrive at the hypergeometric form of Eq.(6),

$$\left[u(1-u)\frac{d^2}{du^2} + (1 - 2u + \lambda_1)\frac{d}{du} + \frac{\lambda_2}{u(1-u)} + \frac{\lambda_3(1-2u)}{u(1-u)}\right]\eta_+^s(u) = 0, \tag{7}$$

with $\lambda_1 = -\frac{\delta s \nu_F}{2m_1}$, $\lambda_2 = \frac{\delta^2 m_0}{4m_1}$, and $\lambda_3 = -\frac{\delta^2 M}{4m_1}$. In the derivation of Eq.(7), we have used identity $\tanh\frac{x}{\delta} = 1 - 2u$. This equation has poles at $u = 0, 1, \infty$ and therefore leads to hypergeometric solutions. Let's set

$$\eta_+^s(u) = u^\alpha(1-u)^\beta f_+^s(u), \tag{8}$$

with

$$\alpha = \frac{\delta}{2}\frac{\sqrt{\nu_F^2 - 4m_1(m_0 - M)} - \nu_F}{2m_1}, \tag{9}$$

$$\beta = \frac{\delta}{2}\frac{\nu_F - \sqrt{\nu_F^2 - 4m_1(m_0 + M)}}{2m_1}. \tag{10}$$

Substituting $\eta_+^s(u)$ into Eq.(7), we arrive at the Gaussian equation

$$u(1-u)f''(u) + [(2\alpha + 1 + \lambda_1) - (2\alpha + 2\beta + 2)u]f'(u) - (\alpha+\beta)(\alpha+\beta+1)f(u) = 0, \tag{11}$$

where we have used identity $\alpha^2 + \lambda_1\alpha + \lambda_3 + \lambda_2 = 0$ and $\beta^2 - \lambda_1\beta - \lambda_3 + \lambda_2 = 0$. Then Eq.(11) has the special solution

$$f(u) = K_1\ {}_2F_1(\alpha+\beta, \alpha+\beta+1, 2\alpha+1+\lambda_1; u), \tag{12}$$

with the hypergeometric function ${}_2F_1$ and a normalized constant K_1. Moreover, from the the boundary conditions $\eta_+^s(x = -\infty) = 0$ and $\eta_+^s(x = +\infty) = 0$, one can find $s = -1$ (see Appendix A for a detailed discussion on the boundary conditions). Finally, we get the solution $\zeta_+(x)$

$$\zeta_+(x) = \eta_+^-(x)\chi_x^- = K_1 u^\alpha (1-u)^\beta\ {}_2F_1(\alpha+\beta, \alpha+\beta+1, 2\alpha+1+\frac{\delta\nu_F}{2m_1}; u)\begin{pmatrix} 1 \\ -1 \end{pmatrix}. \tag{13}$$

Here, we only reserve the sign of s in superscripts.

Next, we solve the eigenequation $H_-\zeta_-(x) = E\zeta_-(x)$ for $k_y = 0$ and $E = 0$,

$$[\nu_F k_x\tilde{\sigma}_y + (m_0 - m_1k_x^2 - M_z)\tilde{\sigma}_z]\zeta_-(x) = 0. \tag{14}$$

In order to solve this differential equation, we use instead of x the variable $g = (1 + e^{-2x/\delta})^{-1}$ and considering the ansatz $\zeta_-(x) = \eta_-^s(x)\chi_x^s$, the Eq.(14) becomes

$$[g(1-g)\frac{d^2}{dg^2} + (1 - 2g + \lambda_1)\frac{d}{dg} + \frac{\lambda_2}{g(1-g)} + \frac{\lambda_3(1-2g)}{g(1-g)}]\eta_-^s(g) = 0, \tag{15}$$

which has the same form as Eq.(7). This allows us to reuse the previous results. To satisfy the boundary conditions $\eta_-^s(-\infty) = 0$ and $\eta_-^s(+\infty) = 0$, we can obtain the wave function of zero energy for H_-,

$$\zeta_-(x) = \eta_-^-(x)\chi_x^- = K_2 g^\alpha(1-g)^\beta \,{}_2F_1(\alpha+\beta, \alpha+\beta+1, 2\beta+1+\frac{\delta\nu_F}{2m_1}; g)\begin{pmatrix}1\\-1\end{pmatrix}, \tag{16}$$

with a normalized constant K_2.

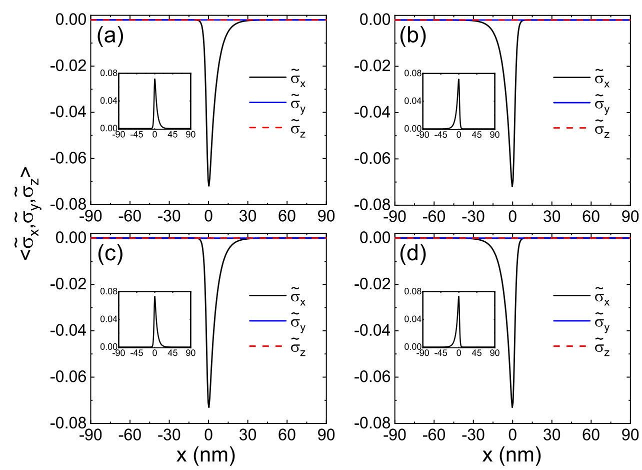

FIG. 3. Distribution of expectation value of $\tilde{\sigma}_x, \tilde{\sigma}_y, \tilde{\sigma}_z$ in the bound state at the DW solved from (a) H_+ and (b) H_- with momentum $k_y = 0$ by numerical calculation. (c) and (d) are the analytic results from $\zeta_+(x)$ and $\zeta_-(x)$ in Eqs.(13) and (16). The insets display probability density of the bound states.

Written in a four-component notation, $\zeta_+(x) = \eta_+^-(x)(1, -1, 0, 0)^T$ and $\zeta_-(x) = \eta_-^-(x)(0, 0, 1, -1)^T$. Figure 3 displays the distributions of the probability density $\zeta_\pm^\dagger(x)\zeta_\pm(x)$ and the expectation value of $\tilde{\sigma}_x, \tilde{\sigma}_y, \tilde{\sigma}_z$ ($\zeta_\pm^\dagger(x)\tilde{\sigma}_i\zeta_\pm(x)$ with $i = x, y, z$) in the bound state $\zeta_\pm$ compared with numerical calculation. Both states are distributed around the DW and decay rapidly away from the center of the DW ($x = 0$) into the bulk. It is obvious that only $\tilde{\sigma}_x$ is non-vanishing and negative which is consist with $s = -1$ as shown in Fig.3. Moreover, the analytical results are well consistent with numerical results.

Now, we consider the perturbation term ΔH by projecting the Hamiltonian $H'(k)$ onto the two zero-energy states leading to the one-dimensional effective Hamiltonian[29,30],

$$H_{\text{eff}} = \begin{pmatrix}\langle\zeta_+|H'|\zeta_+\rangle & \langle\zeta_+|H'|\zeta_-\rangle\\ \langle\zeta_-|H'|\zeta_+\rangle & \langle\zeta_-|H'|\zeta_-\rangle\end{pmatrix}. \tag{17}$$

It can easily be obtained that $\langle\zeta_+|H'|\zeta_+\rangle = \langle\zeta_-|H'|\zeta_-\rangle = -\nu_F k_y$ and the nondiagonal element depends on the type of the DW. For Néel wall, the magnetization vector $\mathbf{M}(x) = M(\text{sech}\frac{x}{\delta}, 0, -\tanh\frac{x}{\delta})$, so $M_\parallel = M\text{sech}\frac{x}{\delta}\mathbf{I}_{2\times2}$ with the 2×2 unit matrix $\mathbf{I}_{2\times2}$. The effective Hamiltonian becomes

$$H_{\text{Néel}}(k_y) = \begin{pmatrix}-\nu_F k_y & \kappa\\ \kappa^* & -\nu_F k_y\end{pmatrix}, \tag{18}$$

where $\kappa = \int \eta_+^{-*}(x)M\text{sech}\frac{x}{\delta}\eta_-^-(x)dx$ is the hybridization of the two states. The excitation spectrum is $E(k_y) = -\nu_F k_y \pm |\kappa|$. These two modes are the nondegenerate chiral modes with a splitting $\Delta k = k_1 - k_2 = 2|\kappa|/\nu_F$ in k_y [blue solid and red dashed lines in the Fig.2(a)]. However, for Bloch wall, $\mathbf{M}(x) = M(0, \text{sech}\frac{x}{\delta}, -\tanh\frac{x}{\delta})$, so $M_\parallel = -iM\text{sech}\frac{x}{\delta}\sigma_z$ and $\langle\zeta_+|H'|\zeta_-\rangle = 0$. The effective Hamiltonian becomes

$$H_{\text{Bloch}}(k_y) = \begin{pmatrix}-\nu_F k_y & 0\\ 0 & -\nu_F k_y\end{pmatrix}. \tag{19}$$

The excitation spectrum is doubly degenerate with $E(k_y) = -\nu_F k_y$ in accordance with Fig. 2(c). At this point, it can be seen that the split between the co-propagating chiral modes results from the x component of the magnetization inside the DW and Δk depends on the type and thickness of the DW.

IV. TRANSPORT OF THE CHIRAL MODES IN TWO-TERMINAL DEVICE

A. Nonequilibrium Green's function method

To study the effect of DW configuration on the transport of the DW of magnetic TI, we construct a two-

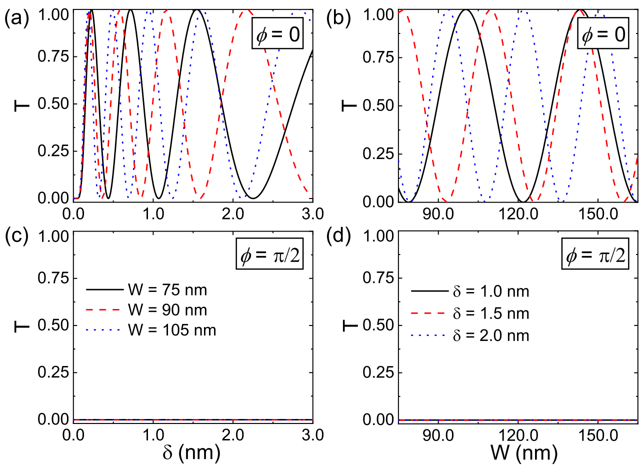

FIG. 4. (a) and (c) The transmission coefficient T versus DW thickness δ for (a) Néel wall ($\phi = 0$) and for (c) Bloch wall ($\phi = \pi/2$) in several widths W for $E = 0$. (b) and (d) T versus width W for (b) Néel wall and (d) Bloch wall in several DW thicknesses δ for $E = 0$.

terminal device [see Fig.1(a)] which contains a DW in the center region and two semi-infinite left and right magnetic TI domains. For low incident energy, the transport occurs via the CESs and Fig.2(b) depicts the transport process. By using the nonequilibrium Green's function method, the transmission coefficients can be obtained from[23,32–34] $T(E) = \mathrm{Tr}[\Gamma_L G^r \Gamma_R G^a]$, with the incident energy E, retarded/advanced Green's function $G^{r/a}(E)$, and line-width function $\Gamma_{L/R}(E)$. In real transport experiments, the two-terminal conductance G can be measured and is related to the transmission coefficients by $G = \frac{e^2}{h}T$ at the low temperature, where e is the electronic charge and h is the Planck constant.

When an electron propagating along the mode a_1 (black arrow from the left terminal) arrives at the trijunction ν_1, it is scattered into the chiral modes c_1 and c_2 in the DW region as shown in Fig.2(b). After the propagation along the DW, the electron is scattered off the trijunction ν_2 and gets into the outgoing modes b_1 and b_2 eventually. Fig.2(d) shows the transmission coefficient T at $E = 0$ as a function of ϕ which specifies the type of the DW. T is the periodic function of ϕ with the period π, so we only show the results for $0 \leq \phi \leq \pi$. It can be observed in Fig.2(d) that for Bloch wall ($\phi = \pi/2$), the transmission coefficient $T = 0$ and remains unchanged with the change in the DW thickness δ. However, deviating from $\phi = \pi/2$, T oscillates between 0 and 1 with the change in ϕ and DW thickness δ, and is symmetric about $\phi = \pi/2$, i.e. $T(\phi) = T(\pi - \phi)$. These results suggest that the current of the device in Fig.1(a) can be switched on or off by changing the magnetization configuration of the DW. Such a switch effect has an underlying application in spintronics, because that the current is completely layer-locked spin-polarized[28,35].

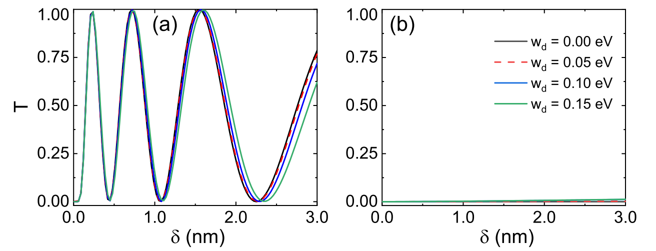

FIG. 5. The transmission coefficient T versus DW thickness δ at the different disorder strengths w_d for (a) Néel wall ($\phi = 0$) and for (b) Bloch wall ($\phi = \pi/2$). The width of the DW is $W = 75$ nm and the other unmentioned parameters are the same as in Fig. 4(a). The curves in (a) and (b) are averaged over up to 100 random disorder configurations. The legend of (a) is the same as in (b).

Let us study the Néel wall and Bloch wall in detail. Figure 4 shows the dependence of transmission coefficient T on the DW thickness δ and device width W. For Néel wall, T approaches zero as the thickness of the DW vanishes [see Fig.4(a)]. With increasing in the thickness of the DW, T oscillates between 0 and 1 for a fixed width W. The thinner the DW is, the faster T oscillates. Moreover, T shows a periodic function of the device width W and the period is small for thick DW [see Fig.4(b)]. These imply that the device with Néel wall exhibits the behavior of a two-path interferometer. However, for Bloch wall, the transmission coefficient T is vanishing regardless of the system parameters [see Fig.4(c,d)]. At this point, we can see that the two different DWs show absolutely different transport behaviors. At the Sec. IVB, based on the effective Hamiltonian Eqs.(18 and 19), we will construct the scattering matrix S of the two-terminal device to understand the underlying physics.

Moreover, we consider the effect of disorder on the transport in the two-terminal device. With the presence of disorders, on each site the term T_0 in Eq.(2) is changed to $T_0 + w_{\mathbf{i}}\sigma_0\tau_0$, where $w_{\mathbf{i}}$ is uniformly distributed in the range $[-w_d/2, w_d/2]$ with disorder strength w_d. Here, we consider a disordered region with a length of 32.4 nm which completely covers the thickest DW in our calculation. Figure 5 displays the transmission coefficients T versus DW thickness δ at the different disorder strengths w_d. It is apparent that the disorders hardly change the transport properties for both Néel wall [Fig.5(a)] and Bloch wall [Fig.5(b)], even if the disorder strength $w_d = 0.15$eV is much larger than the bulk gap $E_{gap} = 2(M - m_0) = 0.044$eV. This is because the CESs are topologically protected and the chirality of the CESs at the DW is different.

B. Scattering matrix S

To find the scattering matrix which relates the incoming modes to the outgoing modes, we return to the Hamil-

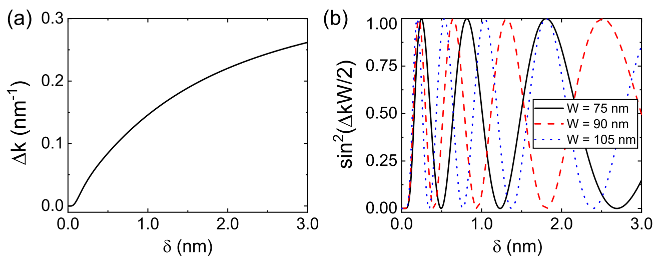

FIG. 6. (a) Momentum difference Δk between the modes $c_{1,2}$ as a function of the thickness δ of the DW for zero energy extracted from the band structure [see Fig.2(a)]. (b) $\sin^2(\Delta kW/2)$ versus the thickness δ for several widths W.

tonian $H'(k)$ [see Eqs.(4 and 5)] to see the origin of the chiral modes $a_{1,2}$ and $b_{1,2}$ in Fig.2(b). For left magnetic TI domain with $\mathbf{M} = (0, 0, M)$, $M_{\parallel} = 0$, H_+ is nontrivial and H_- is trivial. So a_1 and b_1 at the edge can be obtained by solving the Hamiltonian H_+ with open boundary conditions solely, which is similar with the mode ζ_+. On the other hand, for right magnetic TI domain with $\mathbf{M} = (0, 0, -M)$, H_+ is trivial and H_- is nontrivial. Similarly, a_2 and b_2 can be obtained from the Hamiltonian H_-, which is similar with ζ_-. Considering that a_1, b_1 and ζ_+ (a_2, b_2 and ζ_-) are the bound state solutions of the H_+ (H_-) and have the same chirality, at the trijunction ν_1 [see Fig.2(b)], the mode a_1 (a_2) is scattered onto ζ_+ (ζ_-) and at the trijunction ν_2, the mode ζ_+ (ζ_-) is scattered into b_1 (b_2).

For Néel wall, the solutions of the chiral modes on the DW [see Fig.2(b)] can be found as $c_{1,2} = \frac{1}{\sqrt{2}}(\zeta_+ \pm \zeta_-)$ from the Hamiltonian $H_{\text{Néel}}$ in Eq.(18). Thus, the scattering matrix of the trijunction ν_1, $S_{\nu_1} = \frac{1}{\sqrt{2}}(\sigma_x + \sigma_z)$ accounts for the scattering of the incoming modes $a_{1,2}$ onto $c_{1,2}$. Similarly, the scattering matrix describes the trijunction ν_2 is $S_{\nu_2} = S_{\nu_1}$, where the modes $c_{1,2}$ are scattered onto the outgoing modes $b_{1,2}$. The scattering amplitude of the two-terminal device is found by composing the scattering matrices,

$$S = S_{v_2} \begin{pmatrix} e^{ik_1 W} & 0 \\ 0 & e^{ik_2 W} \end{pmatrix} S_{v_1}, \tag{20}$$

where the second matrix contains the contribution of the dynamical phase and $k_{1,2}$ is the momentum of modes $c_{1,2}$. In this case, the incoming electron from the chiral mode a_1 is equally split into CESs c_1 and c_2 at ν_1, then $c_{1,2}$ converge at ν_2 and are finally scattered onto the outgoing modes $b_{1,2}$, which serves as a Mach-Zehnder interferometry.[36,37] From Eq.(20), the transmission coefficient is obtained as $T = \sin^2(\Delta kW/2)$ with $\Delta k = k_1 - k_2$. Figure 6 shows Δk and $\sin^2(\Delta kW/2)$ as functions of the thickness δ of the DW. It can be seen that $\sin^2(\Delta kW/2)$ shows a good consistency with the T of Fig.4(a) and is a periodic function of the width of the device in accordance with Fig.4(b). Moreover, for a general DW defined by ϕ, the hybridization $\kappa \propto \cos\phi$ so that the coefficient $\sin^2(\Delta kW/2)$ is the same for ϕ, $\pi - \phi$, and $\pi + \phi$ [see Fig.2(d)].

For Bloch wall, the co-propagating chiral modes on the wall are doubly degenerate and $c_{1,2} = \zeta_\pm$ which can be obtained from the Hamiltonian H_{Bloch} in Eq.(19). This means that the incoming mode a_1 (a_2) is totally reflected onto b_1 (b_2). This results a zero transmission coefficient which is consistent with Fig.4(c) and (d). At this point, we have well understood the low-energy transport behavior of the device containing a DW based on the effective Hamiltonian.

V. CONCLUSIONS

In summary, we find that the spectrum of the chiral modes is strongly dependent on the detailed configuration of the DW. For Bloch walls, the chiral modes are doubly degenerate, while for Néel walls a split is present. Correspondingly, the devices with different DW configuration show very distinct transport behaviors. In Bloch case, the current through the device vanishes regardless of system parameters. However, in the Néel case, the transmission coefficient of the DW oscillates between zero and unity with changes in system parameters and is determined by the interference between the chiral modes. From the scattering matrix of the device derived from the effective Hamiltonian of the chiral modes, these transport behaviors can be well understood. Moreover, the electrical transport of the CESs is robust against the disorders. These findings may pave a way to control the layer-locked spin-polarized current based on magnetic DWs.

ACKNOWLEDGMENTS

This work was financially supported by National Key R and D Program of China (Grant No. 2017YFA0303301), NBRP of China (Grant No. 2015CB921102), NSF-China (Grant No. 11574007), and the Strategic Priority Research Program of Chinese Academy of Sciences (Grant No. XDB28000000).

Appendix A: Determination of the value of s from boundary conditions

Here, we solve the value of s from the boundary conditions $\eta_+^s(x = -\infty) = 0$ and $\eta_+^s(x = +\infty) = 0$ for the solution shown in Eqs.(8) and (12). For the limit $x \to -\infty$ or $u \to 1$, $1 - u = e^{2x/\delta}/(1 + e^{2x/\delta}) \simeq e^{2x/\delta} \to 0$. We apply the transformation rules for passing over from the argument u to $1 - u$ of the hypergeometric function,

$$
\begin{aligned}
&{}_2F_1(\alpha+\beta,\alpha+\beta+1,2\alpha+1+\lambda_1;u)\\
&=\frac{\Gamma(2\alpha+1+\lambda_1)\Gamma(\lambda_1-2\beta)}{\Gamma(\alpha-\beta+1+\lambda_1)\Gamma(\alpha-\beta+\lambda_1)}\times\ {}_2F_1(\alpha+\beta,\alpha+\beta+1,2\beta+1-\lambda_1;1-u)\\
&+\frac{\Gamma(2\alpha+1+\lambda_1)\Gamma(2\beta-\lambda_1)}{\Gamma(\alpha+\beta)\Gamma(\alpha+\beta+1)}(1-u)^{\lambda_1-2\beta}\times\ {}_2F_1(\alpha-\beta+\lambda_1+1,\alpha-\beta+\lambda_1,-2\beta+1+\lambda_1;1-u).
\end{aligned}
\tag{A1}
$$

With $1-u=e^{2x/\delta}$ and ${}_2F_1(0)=1$, this leads to

$$
\begin{aligned}
\eta_+^s(x)\ &=\ K_1u^\alpha(1-u)^\beta\left\{\frac{\Gamma(2\alpha+1+\lambda_1)\Gamma(\lambda_1-2\beta)}{\Gamma(\alpha-\beta+1+\lambda_1)\Gamma(\alpha-\beta+\lambda_1)}+\frac{\Gamma(2\alpha+1+\lambda_1)\Gamma(2\beta-\lambda_1)}{\Gamma(\alpha+\beta)\Gamma(\alpha+\beta+1)}(1-u)^{\lambda_1-2\beta}\right\}\\
&\to K_1\left\{\frac{\Gamma(2\alpha+1+\lambda_1)\Gamma(\lambda_1-2\beta)}{\Gamma(\alpha-\beta+1+\lambda_1)\Gamma(\alpha-\beta+\lambda_1)}e^{2\beta x/\delta}+\frac{\Gamma(2\alpha+1+\lambda_1)\Gamma(2\beta-\lambda_1)}{\Gamma(\alpha+\beta)\Gamma(\alpha+\beta+1)}e^{2(\lambda_1-\beta)x/\delta}\right\}.
\end{aligned}
\tag{A2}
$$

The boundary condition $\eta_+^s(-\infty)=0$ implies that $\beta<\lambda_1$ and $\beta>0$. From Eq.(10), one can see that the condition $\beta>0$ is satisfied always. From the condition $\beta<\lambda_1$ and $\lambda_1=-\frac{\delta s v_F}{2m_1}$, s can only take -1. On the other hand, for the limit $x\to+\infty$ or $u\simeq e^{-2x/\delta}\to 0$, the solution (12) becomes $f(0)=K_1$ or

$$\eta_+^-(x)\to K_1u^\alpha\simeq K_1e^{-2\alpha x/\delta}.$$

The boundary condition $\eta_+^s(\infty)=0$ implies that $\alpha>0$. From Eq.(9), this condition is satisfied at $M>m_0$.

* sunqf@pku.edu.cn

1. M.Z. Hasan and C.L. Kane, Rev. Mod. Phys. **82**, 3045 (2010).
2. X.-L. Qi and S.-C. Zhang, Rev. Mod. Phys. **83**, 1057 (2011).
3. C.-X. Liu, X.-L. Qi, X. Dai, Z. Fang, and S.-C. Zhang, Phys. Rev. Lett. **101**, 146802 (2008).
4. R. Yu, W. Zhang, H.-J. Zhang, S.-C. Zhang, X. Dai, and Z. Fang, Science **329**, 61 (2010).
5. C.-Z. Chang, J. Zhang, X. Feng, J. Shen, Z. Zhang, M. Guo, K. Li, Y. Ou, P. Wei, L.-L. Wang, Z.-Q. Ji, Y. Feng, S. Ji, X. Chen, J. Jia, X. Dai, Z. Fang, S.-C. Zhang, K. He, Y. Wang, L. Lu, X.-C. Ma, Q.-K. Xue, Science **340**, 167 (2013).
6. J.G. Checkelsky, R. Yoshimi, A. Tsukazaki, K.S. Takahashi, Y. Kozuka, J. Falson, M. Kawasaki, and Y. Tokura, Nat. Phys. **10**, 731 (2014).
7. X. Kou, S.-T. Guo, Y. Fan, L. Pan, M. Lang, Y. Jiang, Q. Shao, T. Nie, K. Murata, J. Tang, Y. Wang, L. He, T.-K. Lee, W.-L. Lee, and K.L. Wang, Phys. Rev. Lett. **113**, 137201 (2014).
8. A.J. Bestwick, E.J. Fox, X. Kou, L. Pan, K.L. Wang, and D. Goldhaber-Gordon, Phys. Rev. Lett. **114**, 187201 (2015).
9. A. Kandala, A. Richardella, S. Kempinger, C.-X. Liu, and N. Samarth, Nature Commun. **6**, 7434 (2015).
10. C.-Z. Chang, W. Zhao, D.Y. Kim, H. Zhang, B.A. Assaf, D. Heiman, S.-C. Zhang, C. Liu, M.H.W. Chan, and J.S. Moodera, Nat. Mater. **14**, 473 (2015).
11. C.-X. Liu, S.-C. Zhang, and X.-L. Qi, Annu. Rev. Condens. Matter Phys. **7**, 301 (2016).
12. A. Hubert and R. Schäfer, *Magnetic Domains: The Analysis of Magnetic Microstructures* (Springer, Berlin, 1998).
13. N.A. Spaldin, *Magnetic Materials: Fundamentals and Applications* (Cambridge University Press, Cambridge, 2014).
14. A. Thiaville, S. Rohart, É. Jué, V. Cros, and A. Fert, Europhys. Lett. **100** 57002 (2012).
15. G. Chen, J. Zhu, A. Quesada, J. Li, A.T. NDiaye, Y. Huo, T.P. Ma, Y. Chen, H.Y. Kwon, C. Won, Z.Q. Qiu, A.K. Schmid, and Y.Z. Wu, Phys. Rev. Lett. **110**, 177204 (2013).
16. G. Chen, T. Ma, A.T. NDiaye, H. Kwon, C. Won, Y. Wu, and A.K. Schmid, Nature Commun. **4**, 2671 (2013).
17. M.D. DeJong and K. L. Livesey, Phys. Rev. B **92**, 214420 (2015).
18. K. Yasuda, M. Mogi, R. Yoshimi, A. Tsukazaki, K.S. Takahashi, M. Kawasaki, F. Kagawa, and Y. Tokura, Science **358**, 1311 (2017).
19. I.T. Rosen, E.J. Fox, X. Kou, L. Pan, K.L. Wang, and D. Goldhaber-Gordon, npj Quantum Materials **2**, 69 (2017).
20. S.S.P. Parkin, M. Hayashi, L. Thomas, Science **320**, 190 (2008).
21. J. Wang, B. Lian, and S. C. Zhang, Phys. Rev. B **89**, 085106 (2014).
22. J. Wang, Phys. Rev. B **94**, 214502 (2016).
23. S. Datta, *Electronic Transport in Mesoscopic System*, (Cambridge University Press, Cambridge, 1995).
24. C.-Z. Chen, J.J. He, D.-H. Xu, and K.T. Law, Phys. Rev. B **96**, 041118 (2017).
25. C.-Z. Chen, Y.-M. Xie, J. Liu, P.A. Lee, and K.T. Law, Phys. Rev. B **97**, 104504 (2018).
26. Y.-H. Li, J. Liu, H. Liu, H. Jiang, Q.-F. Sun, and X. C. Xie, Phys. Rev. B **98**, 045141 (2018).
27. X.-L. Qi, Y.-S. Wu, and S.-C. Zhang, Phys. Rev. B **74**, 085308 (2006).
28. R.-X. Zhang, H.-C. Hsu, and C.-X. Liu, Phys. Rev. B **93**, 235315 (2016).
29. S.-Q. Shen, *Topological Insulators*, (Springer, Berlin, 2012).
30. J. Wang, Phys. Rev. B **98**, 024519 (2018).

[31] S. Flügge, *Practical Quantum Mechanics* (Springer, Berlin, 1999).
[32] W. Long, Q.-F. Sun, and J. Wang, Phys. Rev. Lett. **101**, 166806 (2008).
[33] Q.-F. Sun and X.C. Xie, Phys. Rev. Lett. **104**, 066805 (2010).
[34] Y.-F. Zhou, Z. Hou, Y.-T. Zhang, and Q.-F. Sun, Phys. Rev. B **97**, 115452 (2018).
[35] J. Wu, J. Liu, and X.-J. Liu, Phys. Rev. Lett. **113**, 136403 (2014).
[36] R. Ilan, F. de Juan, and J.E. Moore, Phys. Rev. Lett. **115**, 096802 (2015).
[37] Y. Ji, Y. Chung, D. Sprinzak, M. Heiblum, D. Mahalu, and H. Shtrikman, Nature **422**, 415 (2003).